ACSNANO

www.acsnano.org

ARTICLE

Scalable Synthesis of Crystalline One-Dimensional Carbon Nanothreads through Modest-Pressure Polymerization of Furan

Steven Huss, Sikai Wu, Bo Chen, Tao Wang, Margaret C. Gerthoffer, Daniel J. Ryan, Stuart E. Smith, Vincent H. Crespi, John V. Badding, and Elizabeth Elacqua*

Cite This: https://dx.doi.org/10.1021/acsnano.0c10400 Read Online

ACCESS | Metrics & More | Article Recommendations | Supporting Information

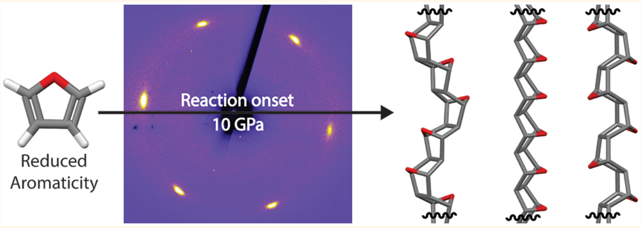

ABSTRACT: Carbon nanothreads, which are one-dimensional sp^3-rich polymers, combine high tensile strength with flexibility owing to subnanometer widths and diamond-like cores. These extended carbon solids are constructed through pressure-induced polymerization of sp^2 molecules such as benzene. Whereas a few examples of carbon nanothreads have been reported, the need for high onset pressures (≥17 GPa) to synthesize them precludes scalability and limits scope. Herein, we report the scalable synthesis of carbon nanothreads based on molecular furan, which can be achieved through ambient temperature pressure-induced polymerization with an onset reaction pressure of only 10 GPa due to its lessened aromaticity relative to other molecular precursors. When slowly compressed to 15 GPa and gradually decompressed to 1.5 GPa, a sharp 6-fold diffraction pattern is observed *in situ*, indicating a well-ordered crystalline material formed from liquid furan. Single-crystal X-ray diffraction (XRD) of the reaction product exhibits three distinct *d*-spacings from 4.75 to 4.9 Å, whose size, angular spacing, and degree of anisotropy are consistent with our atomistic simulations for crystals of furan nanothreads. Further evidence for polymerization was obtained by powder XRD, Raman/IR spectroscopy, and mass spectrometry. Comparison of the IR spectra with computed vibrational modes provides provisional identification of spectral features characteristic of specific nanothread structures, namely *syn*, *anti*, and *syn*/*anti* configurations. Mass spectrometry suggests that molecular weights of at least 6 kDa are possible. Furan therefore presents a strategic entry toward scalable carbon nanothreads.

KEYWORDS: *polymerization, carbon nanothreads, high-pressure, polymer, Diels–Alder*

Carbon-based nanomaterials including zero-dimensional fullerenes,[1,2] one-dimensional (1D) nanotubes[3,4] and nanohoops,[5−7] two-dimensional graphanes[8,9] and covalent organic frameworks (COFs),[10−12] have garnered interest in the scientific community owing to their excellent chemical and physical properties. 1D-extended carbon-based solids have emerged as intriguing nanomaterials for a diverse range of applications such as fibers, nanocomposites, field-emission applications, thermal connections, and thermal management.[13−15] Organic sp^3-bonded polymeric nanothreads are of particular interest owing to their high aspect ratio diamond-like core, which is imagined to give them a combination of high tensile strength and polymer flexibility.

1D-polymeric nanothreads have been synthesized from the pressure-induced polymerization of aromatic molecules (*e.g.*, benzene, pyridine, and thiophene) upon compression to 23−30 GPa.[16−21] Theory indicates that such materials possess extraordinary tensile strength, flexibility, and tunable band gaps,[22−25] with potential utility in applications ranging from catalysis and structural materials to biology.[26] However, these reactions are not easily scalable due to the high reaction pressures needed to form covalent bonds. This presents a significant bottleneck to the large-scale production of these value-added polymers.

Production of nanothreads from molecules other than benzene suggests that physical organic principles such as electron delocalization and steric/substitution effects govern their reaction, as opposed to topochemistry.[27] Nuclear magnetic resonance spectroscopic studies suggest that nanothread formation begins with a [4 + 2] cycloaddition between

Received: December 12, 2020
Accepted: January 12, 2021

two molecules of furan, leading to regions of sp^3 character, along with further polymerizable sp^2 segments.[28,29] If so, molecules with decreased electron delocalization and thus lessened aromatic character will lead to more mild reaction conditions, thus achieving product scalability.

Benzene and pyridine are stable molecules not known for aromaticity-breaking reactions due to their intrinsic delocalized resonance energies of ~0.060 eV per π electron.[30,31] Such resonance energies are defined by the extra stability a molecule possesses resulting from electrons being spread over the entirety of the molecule. Molecules with larger resonance energies >0.050 eV are still reactive; however, these are often substitution-based reactions that restore the delocalized network. Benzene and pyridine are cyclic arrays whose stability arises from large delocalization; thus, they are not typically vulnerable to addition reactions, likely necessitating higher pressures to break this array and induce reactivity in nanothread-forming reactions. Indeed, calculated activation barriers for nanothread initiation (*e.g.*, dimer formation) in benzene and pyridine exceed 58 kcal mol^{-1}[32] (the barrier for benzene nanothread initiation has been calculated and can be found in Figure S1); thus, high reaction pressures are necessitated for reaction, and product scalability remains a challenge. Recently, an aryl/perfluoroaryl supramolecular synthon was produced that exhibited a lower reaction onset pressure due to favorable noncovalent interactions; this led to a lowered activation barrier for nanothread synthesis.[33] To realize lower reaction pressure, it is important to identify molecules, or co-crystal systems, prone to addition reactions that have a lessened barrier of activation.

In this regard, furan is a high-value target. Similar to benzene and pyridine, the structure does comprise a cyclic array of π-orbitals, yet the added stability from them is far less. The electronegativity of the oxygen atom in furan reduces this energy to only 0.007 eV per electron, meaning it is vulnerable to addition reactions.[34] Furan is also well-established as a reactant *par excellence* for cycloaddition reactions, which is important given nanothread formation is likely predicated on a series of [4 + 2] cycloadditions.[35] Combined, these features result in a lessened aromatic character. We hypothesized that furan should favorably lower the activation energies required for [4 + 2] cycloaddition reaction, which is the likely initiation step for nanothread formation, thus aiding in product scalability. Despite this, prior approaches to polymerize furan led to an amorphous product likely with a high degree of cross-linking.[36] The amorphous product and high degree of cross-linking can likely be attributed to fast compression to 47 GPa, which is exceedingly high, and enabling lesser-defined reactions to result.

Herein, we report the synthesis of well-ordered crystalline furan-derived nanothreads produced by slow compression and decompression of single-crystalline and powder furan with a reaction onset at 10 GPa. This system and approach produces sp^3-bonded crystalline carbon nanothreads at ambient temperature with the lowest reported reaction pressure to date, which is an important step toward the scalable synthesis of extended carbon solids. In addition, the resultant polymers would feature polar ethers in each repeat unit (Figure 1), with several distinct conformers that align overall polarity transverse or longitudinal to the thread axis. The presence of oxygen may facilitate postpolymerization processing such as intercalation with metals and/or Lewis acids, as well as exfoliation. Both of these are prerequisites for applications as nanocomposites or conducting thin-film materials.

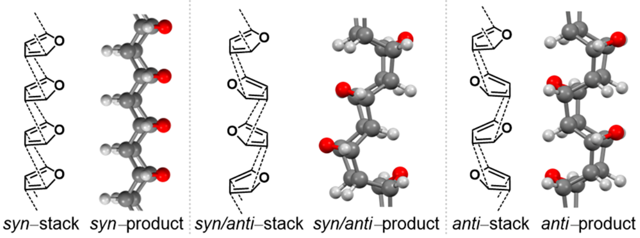

Figure 1. Regiochemical outcomes of continuous [4 + 2] cycloadditions of furan affording *syn*-, mixed *syn*/*anti*-, and *anti*-configured furan nanothreads.

RESULTS AND DISCUSSION

To gain insight into the effect of electron delocalization on nanothread formation, we calculated the [4 + 2] activation barrier for the dimerization of furan. That barrier was determined to be 35 kcal mol $^{-1}$, whereas ambient Diels–Alder reactions (*e.g.*, cyclopentadiene and ethylene) exhibit activation barriers around 21 kcal mol^{-1}.[37] Benzene and pyridine have been shown to polymerize into crystalline nanothreads; however, their high degrees of aromatic character result in large barriers greater than 46 kcal mol^{-1}. The combined calculations suggest that furan is a system which should be expected to react at a much lower pressure.

To probe the importance of furan's lowered aromatic character on its reaction onset pressure, we performed two independent compressions of single-crystal and powder furan in diamond anvil cells (Figures 2 and 3). Liquid furan was

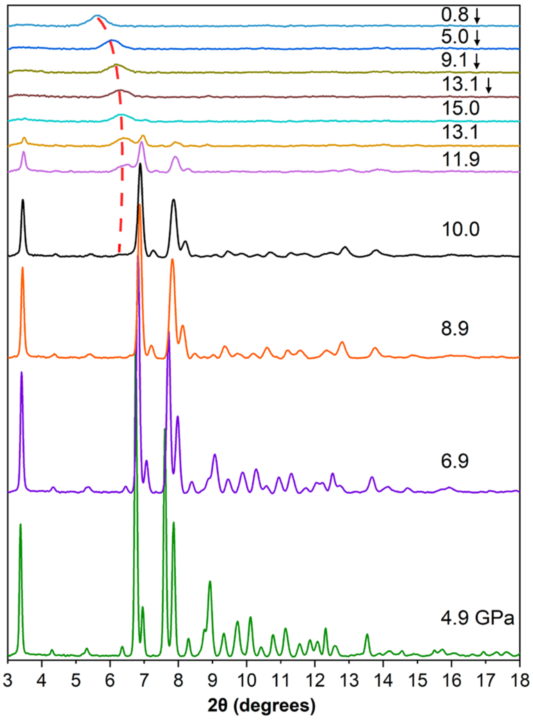

Figure 2. *In situ* synchrotron powder X-ray diffraction (PXRD) of the slow compression and decompression (↓) of furan to 15 GPa. PXRD patterns show evolution of furan and nanothread reflection (red dashed line) during high-pressure synthesis.

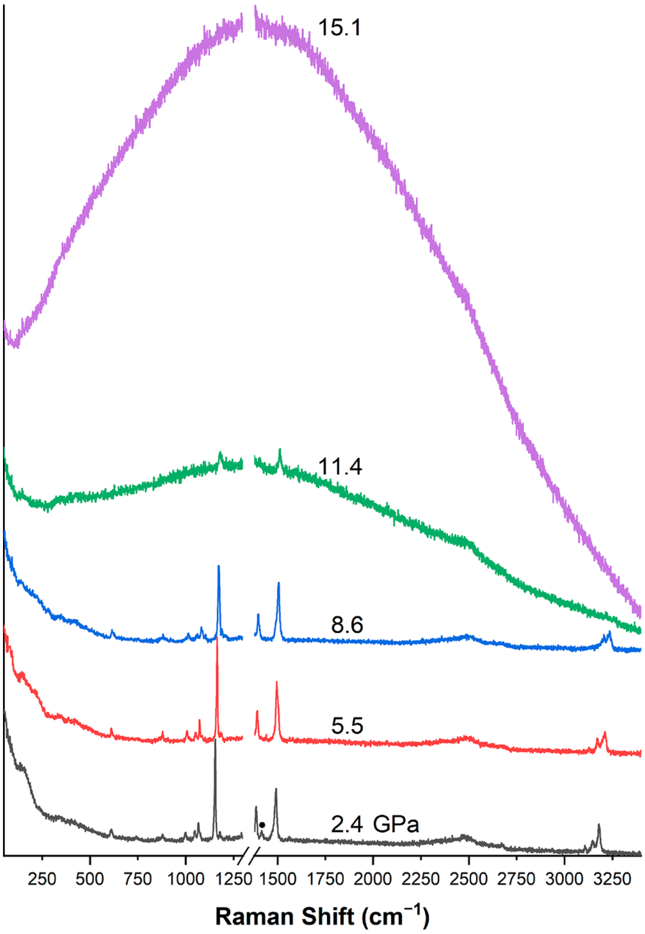

Figure 3. *In situ* Raman spectroscopy during slow compression. The dot indicates the ruby Raman shift used for calibration. The line break is to cut out the intense diamond mode.

loaded into a double-stage membrane diamond anvil cell[38] and slowly compressed at room temperature (298 K) to 15 GPa over a period of 10−12 h. The compression rate began at 4.2 GPa/hour from ambient pressure up to 8 GPa; the rate was then reduced to 1.8−2.4 GPa/hour above 8 GPa and slowed again to 0.6−1.2 GPa/hour above 11 GPa. Liquid furan solidified at ca. 1.4 GPa.[36] The reaction was held at 15 GPa for 2 h and released to ambient pressure over 10−12 h at the same rates as compression. Upon carefully opening the cell, an off-white solid filled the reaction chamber.

In situ synchrotron powder X-ray diffraction (Figure 2) revealed a new diffraction peak at 10 GPa, reflecting the onset of reaction. This diffraction peak grew in intensity up to 15 GPa and persisted on decompression. *In situ* Raman Spectroscopy (Figure 3) provides further evidence of furan polymerization in the same pressure range. At lower pressures (*i.e.*, 2.4 GPa), the characteristic Raman modes of Phase IV solid furan[36] are observed: ring bending (879, 1048 cm^{-1}), ring stretching (1048, 1154, 1388, 1490, 1563 cm^{-1}), C−H bending (611, 743, 860, 998, 1067, 1179 cm^{-1}), and C−H stretching (3090−3200 cm^{-1}). These frequencies increase with increasing pressure. The lattice modes are largely superimposed in the tail of the laser excitation line and appear as a structureless broad band. Above ca. 4 GPa, a phase transition from the orientationally disordered Phase IV to the ordered Phase III begins (Figure S2), as previously found through *in situ* infrared spectroscopy.[36] This indicates that solid furan at this pressure is still somewhat disordered; given the phase transition is slow, a mix of these two phases appears to exist up to 15 GPa. Around 11.4 GPa, the fluorescence background increased, indicating the onset of a chemical transformation and is consistent with the formation of sp^3-based connectivity. The Raman modes weakened dramatically at 11.4 GPa and disappeared at 15.1 GPa.

In Situ X-ray Diffraction of Furan Nanothreads. *In situ* single-crystal X-ray diffraction during slow decompression exhibits a distinct near-6-fold diffraction pattern (Figure 4a) similar to those seen in previously synthesized nanothreads.[16−18,39,40] The furan-derived sample yields sharper spots than do many other nanothreads in the literature. Three similar but distinct *d*-spacings are observed at 4.75, 4.85, and 4.90 Å, relating to a near-hexagonal structure. Furan nanothreads are expected to have a noncircular cross-section due to the reduced symmetry of the furan ring compared with benzene, consistent with a modest deviation from true 6-fold symmetry. (Cylinders have an isotropic cross−section and its densest packing should result in a hexagonal packing. The *syn*, *anti*, and *syn/anti* furan nanothread structures simulated through [4 + 2] cycloaddition pathways all have elliptical cross-sections. The packing of ellipses is a more complex situation and more packing arrangements can be built; see Figure S3.) Previously reported reaction products from the compression of furan have been amorphous,[36] likely due to cross-linking caused by fast compression and decompression to higher pressures.[16,17]

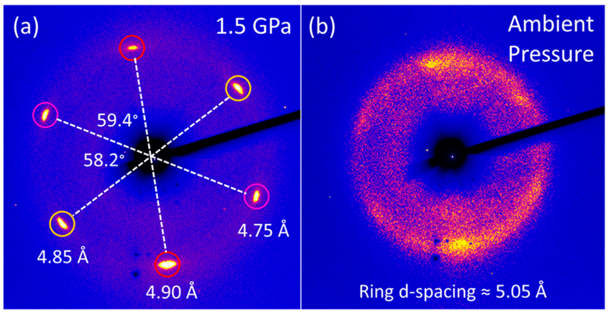

Figure 4. X-ray diffraction collected down the nanothread crystal axis on decompression at (a) 1.5 GPa and (b) ambient pressure.

Upon decompression from 1.5 GPa to ambient pressure (Figure 4b), the distinct 6-fold spots indicative of high order transform into a lumpy ring at 5.05 Å, with only vestiges of the original near-hexagonal spots now at expanded *d*-spacings of 5.09−5.24 Å. Factors contributing to this marked transformation could include (i) mechanical relaxation of defects and/or *syn* regions in the backbone; (ii) loss of crystallinity upon volatilization of unreacted furan molecules that may form an integral part of the overall packing; (iii) melting of unreacted furan changing the stress conditions on nanothread crystallites; or (iv) the mechanical opening of the DAC causing the crystal to break into smaller crystallites. In this regard, we note that long-range translational order in two dimensions is delicate, especially for packings with nonbonded interactions between constituents, and thus may be prone to disruptions that disturb this order. Understanding the origin of this structural transformation remains a topic of future interest.

Simulated Diffraction and Nanothread Packing. The experimental interplanar spacings for these three Friedel pairs were compared to simulations performed at 0 K and 1.5 GPa for packed furan nanothreads similar to prior analyses of benzene and pyridine nanothreads[17,18] (the SI provides all simulated nanothread packings). Furan nanothreads are expected to be more elliptical in cross section than benzene and pyridine threads (Figure S3). We modeled their packing as a 2D packing of ellipses.[41] A thorough examination of possible packings of ellipses led to the identification of three dense packing structures wherein each ellipse has six touching neighbors; these hexagonal packings are particularly appealing here because of the high formation pressure of nanothreads. Three types of furan nanothreads—*syn*, *anti*, and mixed *syn/anti* (Figure 1)—are the simplest outcomes of successive [4 + 2] cycloadditions; these were packed into the three dense-packed patterns and relaxed at 1.5 GPa.

Good agreement between experiment and the predicted interplanar spacings was obtained for the (*anti*)-B-2-b and (*anti*)-C-2-a packings (Figure 5, notation explained in the SI).

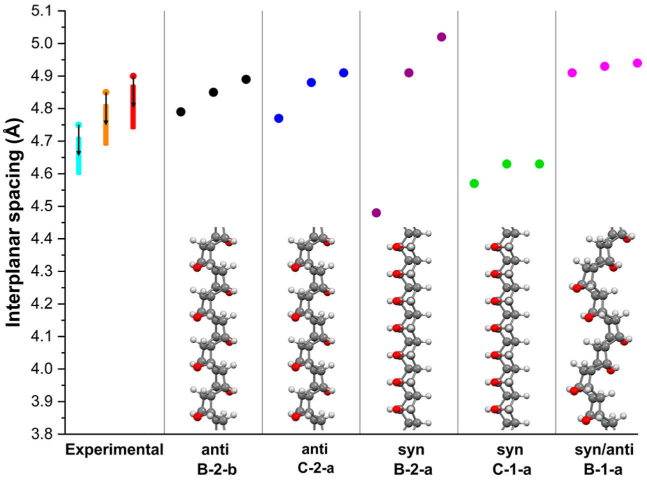

Figure 5. Experimentally observed *d*-spacings of each Friedel pair at 1.5 GPa and room temperature compared to simulated *d*-spacings. The bars indicate the estimated range for a 1−3% thermal contraction to facilitate the comparison to the simulated data performed at 0 K.

These two are the lowest energy packings of all the relaxed (*anti*) packings; they also have the smallest volume per C_4H_4O unit (122 Å^3 and 123 Å^3, respectively). In addition, the angles between the Friedel pairs of the (*anti*)-C-2-a packing closely matched experimental data (Figure S8).

A mixed (*syn/anti*) structure cannot be ruled out, although at least one *d*-spacing of such packings typically exceeds experiment, since (*syn/anti*) has a larger cross-section than (*anti*) and (*syn*). The B-1-a conformation most closely compares to the experimental *d*-spacings and is also the lowest energy of all (*syn/anti*) packings. In contrast, the all-(*syn*) packings are generally too compact along at least one direction, as they have the smallest cross-section of the three conformations; the two closest are shown in Figure 5. Packings of the (*syn*) conformation are generally higher in energy than those of the (*anti*) and (*syn/anti*) conformations, presumably due to steric repulsion of the oxygen atoms.

These comparisons cannot rule out some degree of mixed (*anti*) and (*syn/anti*) conformation along the nanothread axis—note that such mixtures preserve the long axis of the elliptical cross-section and thus remain consistent with the observation of a clear deviation from hexagonal crystal symmetry. They are also accessible along a [4 + 2] cycloaddition pathway, whereas a radical pathway is not expected to preserve a consistent elliptic long axis. If the orientation of the elliptical long axis were to wander, X-ray diffraction would show a pseudohexagonal 6-fold with arcs instead of the observed relatively sharp spots.

The relaxed (*anti*)-C-2-a and (*anti*)-B-2-b packings shown in Figure 6a,b have very different unit cells. Nevertheless, they are both consistent with the experimental single-crystal X-ray diffraction. The monoclinic (*anti*)-C-2-a packing can be viewed as a pseudohexagonal ($\gamma = 121°$) arrangement with the center thread slightly off angle, while the rectangular unit cell of (*anti*)-B-2-b has layers of threads of alternating orientation within an overall pseudohexagonal array.

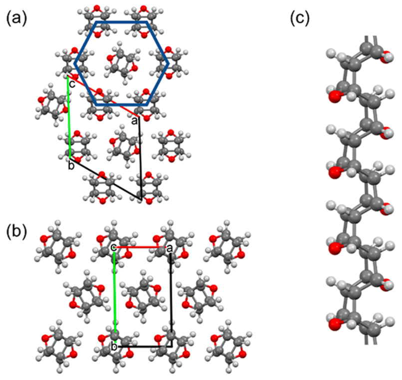

Figure 6. Simulated furan packings at 0 K and 1.5 GPa: (a) View down the *c*-axis of the relaxed (*anti*)-C-2-a; (b) View down the *c*-axis of the relaxed (*anti*)-B-2-b; (c) view perpendicular to the *c*-axis of the (*anti*)-furan nanothread.

These results can be compared to prior X-ray diffraction measurements of thiophene-derived nanothreads, which are well-described by a monoclinic *anti* or *syn/anti* packing.[19] In thiophene-derived threads the steric penalty for *syn* is much larger than for *anti* or *syn/anti*, presumably due to sulfur being larger than oxygen.

Ex Situ Characterization of Furan Nanothreads. Previously reported amorphous polymerized furan containing O−H bonds, alkyl polyether segments, and C═O bonds (a-C:H:O) formed from the uncontrolled compression of furan has a broad infrared (IR) spectrum.[36] The spectrum is relatively featureless from 500 to 700 cm^{-1} and has a large hump from 800 to 1600 cm^{-1}. In comparison, the recovered solid from the slow compression to 15 GPa has more and narrower absorbance peaks (Figure 7), suggesting a well-ordered product. The peaks at 604, 834, 867, 993, 1140, 1169, 1258, 1281, 1485 cm^{-1} of the recovered material resembled those of liquid furan.[42,43] The most prominent feature in the IR spectrum of the recovered solid was the peak between 2800−3060 cm^{-1}, indicative of sp^3 C−H stretching. This provides further evidence that unsaturated furan reacted to form a sp^3-bonded carbon- and oxygen-based polymer. Weak bands between 3060−3180 cm^{-1} are assigned to sp^2 C−H stretching, as well as a mode at 1610 cm^{-1} indicative of C═C stretching; these may arise from unreacted furan,[42] dimers, or oligomers of furan, sp^2-bonded carbon in amorphous side products, and/or defects along the nanothreads. A broad mode centered at 3470 cm^{-1} and a peak at 1718 cm^{-1} were assigned to O−H and C═O stretching, respectively. We attributed these signals to a possible ring opening of furan molecules, as

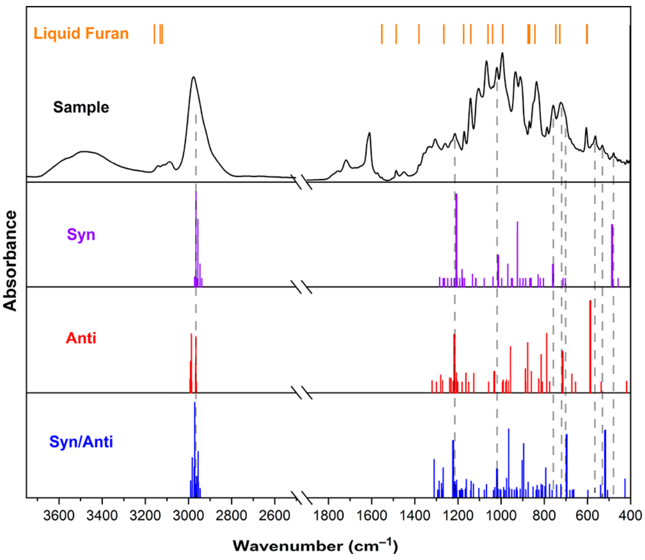

Figure 7. Transmission infrared spectrum of recovered solid and comparison to calculated infrared spectra from three model structure of furan nanothreads. Liquid furan peaks are also overlaid for comparison (ref 42).

observed in prior high-pressure studies.[36,44,45] The peaks between 800–1000 and 1200–1450 cm^{-1} are assigned to C–H alkyl bending modes.

We calculated the IR absorption spectra of the three *syn*, *anti*, and *syn/anti* structures. Of particular interest are several modes from 450 to 760 cm^{-1} that are weak or not observed in amorphous polymerized furan. These new modes divide into two bands. Those from 450 to 620 cm^{-1} occur in the range of calculated C–O–C wagging vibrations of *syn*, *anti*, and *syn/anti* conformers. These modes are diagnostic of thread structure, since *syn*- and *anti*-array oxygen atoms wag in different ways along the thread backbone. The mode at 478 cm^{-1} aligns with a prominent mode at 483 cm^{-1} in the calculated IR spectrum of *syn* furan-derived nanothreads. The mode at 530 cm^{-1} is close to a calculated 518 cm^{-1} mode of the *syn/anti* thread. The modes at 562 and 604 cm^{-1} are in the range of a mode at 587 cm^{-1} of the *anti* nanothread structure; however, the peak at 604 cm^{-1} may have some contribution from unreacted furan.[42] This moderate degree of alignment is consistent with the possibility of a mixture of *syn* and *anti* along the thread backbone. The band of modes from 650 to 760 cm^{-1} is in particularly close alignment with calculated nanothread breathing modes, with the calculated *syn* breathing mode being highest in frequency and the *syn/anti* mode falling just below the *anti* mode, in agreement with the observed shoulder on the left side of the asymmetric experimental peak near 700 cm^{-1}. Additional modes at 1018 cm^{-1} (symmetric C–O stretching) and 1213 cm^{-1} (antisymmetric C–O stretching and/or C–H bending) in the recovered nanothread aligns well with intense modes present with the calculated *syn*, *anti*, and *syn/anti* nanothreads. The modes between 800 and 1000 cm^{-1} are less characteristic of a specific nanothread structure or may involve more complex structural motifs.

The furan nanothreads that are formed are likely a mixture of different thread types. This could be mixtures of pure nanothreads (*i.e.*, a mixture of *syn*, *anti*, and *syn/anti* nanothreads in the crystals) or a mixture of nanothreads along the axis of the thread (*i.e.*, portions of one thread being *syn*, *anti*, and *syn/anti*). This is consistent with observations from transmission electron microscopy of benzene-derived nanothreads[46] as well as the simulations of XRD data (*vide supra*).

X-ray photoelectron spectroscopy (XPS) provided evidence that a largely saturated carbon solid was recovered (Figure S9). The C/O ratio in the recovered solid was 6.2:1 by XPS, reflecting some loss of oxygen during the reaction. Assuming that the surface of the recovered solid exhibited the same composition as the bulk material, the disproportionate loss of oxygen when compared to carbon may be from the formation of CO_2, H_2O, O_2, or organic species with more O atoms. The most reasonable molecule lost may be water, since hydroxyl moieties are seen in the recovered solid.

Larger-Scale Synthesis of Furan Nanothreads. The reduced reaction pressure allows for larger (mg) samples to be prepared with a Paris-Edinburgh (PE) press, a 5000-fold increase in product compared to a DAC. For example, if the DAC gasket hole has a radius of 80 μm and a height of 50 μm, the mass of solid produced from complete consumption of furan would be ~950 ng. Thus, to achieve five milligrams of the product using a DAC would take ~5000 compressions. The aforementioned characterization is routine for crystalline threads achieved on the nanogram scale; realization of a scaleup synthesis presents opportunities to further comprehend furan nanothread structure and properties.

Furan nanothreads produced in a PE press show sharp diffraction with a *d*-spacing of 4.96 Å (Figure 8) with a second-order ring at 2.48 Å, likely indicating polycrystalline nature with nanothread crystallites smaller than the 200 μm X-ray spot. Wide-angle X-ray scattering (WAXS) was also performed on the recovered solid from a PE press. The observed diffraction ring (Figure 8) from the bulk sample shows a ring with a *d*-spacing closely matching that of the single-crystal XRD from the fully decompressed recovered solid (Figure 4b), confirming that the bulk sample also contains crystalline furan-derived nanothreads.

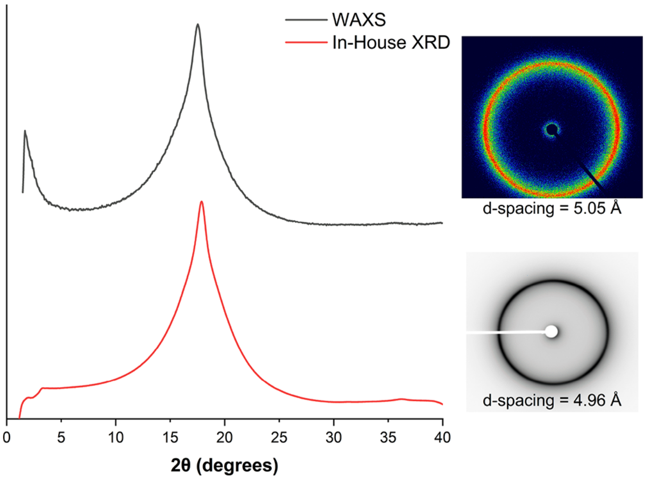

Figure 8. One-dimensional and two-dimensional XRD patterns of furan nanothreads produced in a PE press from wide-angle X-ray scattering and in-house XRD.

The IR spectrum (Figure S11) features stretching modes at 2790–3000 (sp^3 C–H), 3150–3160 (sp^2 C–H), 1550–1690 (C=C), 3430 (O–H), and 1712 cm^{-1} (C=O), similar to those observed through compression in a DAC. The region below 1500 cm^{-1} was more diffuse, likely reflecting a greater degree of disorder, either on-thread or from secondary amorphous component. The double toroidal anvils used in the PE press have a lessened uniaxial pressure distribution:[47,48] this may favor side reactions, as nanothreads often align to a uniaxial pressure axis.[17,18]

PE samples are large enough to perform tests like birefringence. Furan nanothread samples exhibit birefringence under polarized light (Figure 9), consistent with the optical anisotropy expected from a one-dimensional nanostructure.

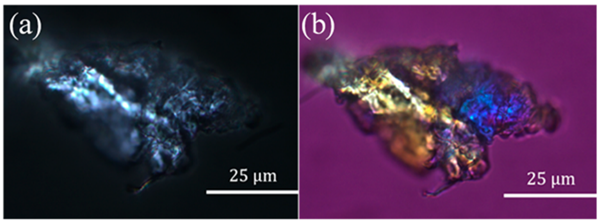

Figure 9. Polarization analysis of a piece of a ~1 mm nanothread sample from a PE press (left) between crossed polars and (right) with a 530 nm full waveplate. A fibrous piece with strong birefringence can be seen at the bottom of the sample.

High-Resolution MALDI Mass Spectrometry. The furan-derived nanothread's molecular weight (MW) distribution and compositional features were determined using high-resolution Fourier transform ion cyclotron resonance mass spectrometry (FT-ICR MS). Due to the limited solubility of the nanothread, matrix-assisted laser desorption/ionization (MALDI) was used to generate gas-phase ions for mass analysis. MALDI MS is a laser-based ionization technique that relies on the incorporation of a small organic matrix to facilitates both desorption of the molecules from the solid sample and their subsequent ionization.[49,50] For the nanothread analysis, 2,5-dihydroxyacetophenone (DHA) was chosen as this matrix is efficient in ionizing large polymers including peptides and proteins.[51,52]

Once prepared, the sample was irradiated with a laser and the mass spectrum was acquired (Figure 10). The most abundant series of peaks, labeled with an orange circle, confirm the presence of furan-derived nanothreads with peak spacings of 68.02 Da (*i.e.*, a single furan molecule) observed between each of the oligomers encompassing the entire mass range. Upon further examination, we detected multiple distributions of nanothreads that are separated by individual furan molecules. The identities of four furan nanothread distributions were determined through accurate mass measurement and can be described as pseudomolecular ions to include a protonated and sodiated species (*e.g.*, $[M + H]^+$ and $[M + Na]^+$ variants), along with derivations of the two.

To further elucidate the structure of the threads, collision-induced dissociation (CID, MS/MS) was completed by dissociating one of the sodiated oligomer molecules and measuring the fragment ions. Figure 11 highlights the fragmentation pattern that is observed. Upon dissociation, we detected a successive loss of furan rings from the parent $[M + Na]^+$ ion down to m/z 227; a loss of nine furan rings. Subtracting two more theoretical furan rings resulted in a remaining mass corresponding to the single sodium ion, highlighted as theoretical peaks in Figure 11. It is this combination of high mass accuracy measurements and fragmentation data that confirmed the identity and structure of the furan-derived carbon nanothreads.

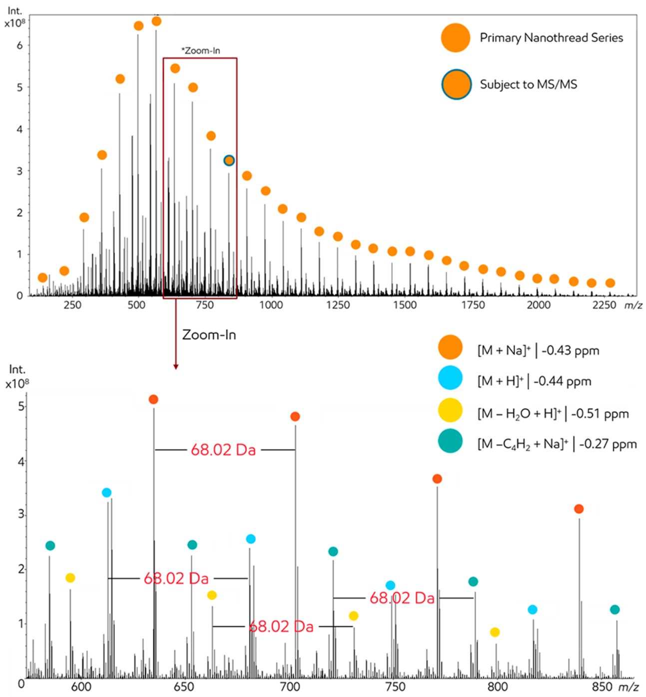

Figure 10. MALDI mass spectrum of the furan carbon nanothreads. The most abundant distribution is highlighted in the top spectrum. A detailed "zoom-in" highlights the multiple forms of nanothread distributions present in the sample. Identifications are based on accurate mass measurements.

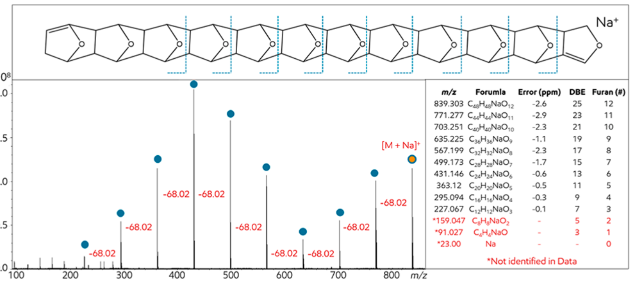

m/z	Forumla	Error (ppm)	DBE	Furan (#)
839.303	$C_{48}H_{48}NaO_{12}$	-2.6	25	12
771.277	$C_{44}H_{44}NaO_{11}$	-2.9	23	11
703.251	$C_{40}H_{40}NaO_{10}$	-2.3	21	10
635.225	$C_{36}H_{36}NaO_9$	-1.1	19	9
567.199	$C_{32}H_{32}NaO_8$	-2.3	17	8
499.173	$C_{28}H_{28}NaO_7$	-1.7	15	7
431.146	$C_{24}H_{24}NaO_6$	-0.6	13	6
363.12	$C_{20}H_{20}NaO_5$	-0.5	11	5
295.094	$C_{16}H_{16}NaO_4$	-0.3	9	4
227.067	$C_{12}H_{12}NaO_3$	-0.1	7	3
*159.047	$C_8H_8NaO_2$	-	5	2
*91.027	C_4H_4NaO	-	3	1
*23.00	Na	-	-	0

*Not identified in Data

Figure 11. CID fragmentation spectrum of a sodiated nanothread is presented. The solid blue circles represent the fragment ions detected after dissociation. The proposed structure is presented and the mass error for each fragment ion is listed.

Finally, to better understand the true MW of the nanothreads, mid-mass and high-mass data were acquired on the FT-ICR. To better visualize the resulting spectra, the low-, mid-, and high-mass spectra were stitched together, and the resulting broadband MS is presented in the Supporting Information (Figure S14). It should be noted that the stitched data appeared as three separate Gaussian-like distributions. This is an artifact of the experiment and likely does not represent the true intensity distribution of the carbon nanothreads. However, we observed a deteriorating signal around 6−7 kDa, suggesting the presence of threads with approximately 100 furan rings. This loss of signal is likely due to limitations in the mass range on the FT-ICR and not the threads themselves. It is important to note that the most prominent species detected is the sodiated oligomer, throughout the entire mass range, which may suggest that sodium could effectively interact with furan-based nanothreads to enable other methods of processing.

https://dx.doi.org/10.1021/acsnano.0c10400
ACS Nano XXXX, XXX, XXX−XXX

CONCLUSIONS

The lower reaction onset for pressure-induced polymerization of furan-derived nanothreads, ~10 GPa, likely reflects the reduced aromaticity of furan compared to benzene or pyridine. These results may aid in selection of precursor molecules for the synthesis of nanothreads at reduced pressures. This reaction yields a primarily sp^3 material with monoclinic order, and mass spectrometry supports the inclusion of up to 100 furan units within the polymer backbone. There is good agreement between experiment and simulated crystal packings and IR response from thread structural models derived from a series of [4 + 2] cycloadditions. These results suggest there is a degree of regioirregularity in oxygen placements across the axis. When the solid is decompressed to ambient pressure, there is a significant lattice dilation and long-range well-defined order is disrupted. This lattice dilation and also polar moieties on the thread backbone may be helpful in their subsequent dissolution and processing.

As furans can be produced from biomass in large quantities, polymers based on them are being pursued with the desire to sustainably transform abundant aromatics into high-value products. While the 10 GPa reaction onset reported here is the lowest achieved thus far for an ordered product, enhanced protocols that exploit photochemistry, thermal treatment, or catalysis might further lower the required pressure and also provide avenues to control regioregularity in the resultant polymers.

EXPERIMENTAL METHODS

Materials and Synthesis. A symmetric diamond anvil cell (DAC) with a 500 μm culet (type IIA diamonds) and a spherical seat diamond anvil cell (DAC) with a 250 μm culet (Washington diamonds) were used for the synthesis of furan nanothreads. Stainless steel gaskets were indented to 45−55 μm thickness and a 100−110 μm (for spherical seat DAC) and 160 μm (for symmetric diamond anvil cell) diameter sample hole was drilled.[53] Pressure was determined *in situ* by ruby fluorescence.[54] Liquid furan (≥99% from Sigma-Aldrich) was filtered through basic alumina immediately prior to loading in the gasket hole at room temperature in order to remove the butylated hydroxytoluene (BHT) used as an inhibitor. Powder furan was loaded by freezing a small amount of furan, placing the solid on top of the gasket hole, and using the diamonds of the DAC to crush the solid into the hole. Single crystals of furan were grown by first loading liquid furan into the DAC. The pressure was increased until the furan froze. The pressure was slowly decreased until the solid furan began to melt. When there were a few small crystallites left of solid furan, the pressure was slowly increased to grow the furan single crystals.

Two sets of gas membranes and digital gas controllers were used to control the rates of compression and decompression. Both compression and decompression proceeded over 10−12 h between ~1.5 and 15 GPa. It was held at 15 GPa for 2 h. The compression rate began at 4.2 GPa/h from up to 8 GPa and then was reduced to 1.8−2.4 GPa/h above 8 GPa and slowed again to 0.6−1.2 GPa/h above 11 GPa, with the same rates for decompression.

We used the same filtered furan for larger scale syntheses in a V7 PE press.[55] Furan was loaded into encapsulated stainless-steel gaskets. Liquid nitrogen was used to freeze the liquid furan into a solid to ensure the gaskets were fully filled without trapped atmosphere; the evaporated nitrogen gas further helped to exclude oxygen and water from the atmosphere of the loading container. The samples were then placed into a V7 PE press equipped with double-toroid polycrystalline diamond anvils.[47] The system was driven by an automatic oil syringe pump, allowing for controlled pressure ramps. A pressure-load calibration curve was used from previously reported data for the double-toroid anvil design.[56] The sample pressure was approximately 15 GPa at an oil pressure of 692 bar. When the oil pressure reached 547 bar, a slow rate of increase (1 bar/min) was employed in both compression and decompression. Using the PE press, 4−5 mg of solid can be produced consistently between runs when loading 21 μL of furan into the gasket. This gives a yield of approximately 20−25% by mass, assuming no furan volatilizes upon loading.

***In Situ* Raman Spectroscopy.** Raman spectra were obtained by a Renishaw inVia Raman spectrometer, with a microscope attachment, using a 633 nm laser focused through a 20× long working distance objective (NA = 0.35) into the DAC. A minimal laser power of 100 μW was used to avoid any kind of sample damage or side reactions.

X-ray Diffraction. The gasket samples recovered to ambient pressure from the DAC were investigated at HPCAT beamline 16-BM-D at the Advanced Photon Source. At 16-BMD, a 20 keV 5 × 5 μm monochromatic beam was focused on the sample and diffractions patterns were collected on a MAR345 image plate detector.

X-ray powder diffraction patterns were collected at HPCAT beamline 16-BMD. At 16-BMD, a 25 keV 5 × 5 μm monochromatic beam was focused on the sample, and diffraction patterns were collected on a MAR345 image plate detector. Diffractions were collected by rastering over a 50 × 50 μm square in the center while rotating ω by ±25 degrees in 2° steps.

X-ray single crystal diffraction patterns were collected at HPCAT beamline 16-IDB. A 30 keV 5 × 5 μm monochromatic beam was focused on the sample, and diffraction patterns were collected on a Pilatus 1 M detector over $\omega = \pm 29°$ with 1°/step.

X-ray diffraction patterns obtained from samples recovered from the PE press were collected with Cu Kα1 (λ = 1.5418 Å) radiation from a MicroMax-007 rotating anode generator using a Varimax VHF monochromator. The beam diameter was 200 μm and collected on a Mar345 image plate detector. The samples produced in the PE press were collected by placing a piece in between two layers of 2.5 μm thick mylar film.

Two-dimensional diffraction patterns were converted to one-dimensional diffraction patterns using the diffraction software DIOPTAS.[57]

The wide-angle X-ray scattering experiments were performed by using an in-house SAXS/WAXS laboratory system (Xeuss 2.0 HR, Xenocs, France) equipped with a microfocus sealed tube (copper) with X-ray wavelength of 1.54 Å (50 kV, 0.6 mA) and a Pilatus3 R200 K detector with a sample to detector distance of approximately 150 mm. The scattering experiments were collected under vacuum at room temperature, and integrated over a tilted circle profile to convert 2D images into one-dimensional scattering patterns of scattering intensity I(q) (in arbitrary units) versus q (A-1).

Infrared Spectroscopy. We performed mid-IR absorption measurements on the sample recovered from the DAC with a Bruker Vertex V70 spectrometer equipped with a Hyperion 3000 FT-IR microscope. Background spectra were collected of the air, under the same experimental conditions, and subtracted using OPUS software.

MALDI FT-ICR MS. Mass spectrometry was completed on a 15T FT-ICR MS (Bruker Daltonics, Billerica, MA) equipped with a Smartbeam II 2 kHz frequency tripled Nd:YAG (355 nm) laser in positive-ion mode. The matrix 2,5-Dihydroxyacetophenone (DHA) was dissolved in a 9:1 solution of acetonitrile/water to a final concentration of 15 mg/mL. The nanothread (*ca.* 2 mg) was suspended in a small amount of toluene and gently crushed with a spatula. Small pieces of nanothread were aspirated and then deposited onto a MALDI target and allowed to dry. Following, 2 μL of DHA solution was added atop and allowed to dry and cocrystallize with the nanothreads. Data was gathered from m/z 100 to 10000 by acquiring in smaller m/z ranges. The ion optics were tuned so that signal was optimized for sensitivity at low-, mid-, and high-mass regions. Resolving power was approximately 235000 at m/z 400. Laser power was varied from 20−30%, and the number of shots was varied from 50 to 200. The CID experiment was performed by isolating the precursor ions, fragmenting at 20 V energy, and coadding 50 spectra. Formula assignments were made using Compass Data Analysis (Bruker Daltonics).

X-ray Photoelectron Spectroscopy (XPS). XPS experiments were performed using a Physical Electronics VersaProbe II instrument equipped with a monochromatic Al k_α X-ray source ($h\nu$ = 1,486.7 eV) and a concentric hemispherical analyzer. Charge neutralization was performed using both low energy electrons (<5 eV) and argon ions. The binding energy axis was calibrated using sputter cleaned Cu (Cu 2p3/2 = 932.62 eV, Cu 3p3/2 = 75.1 eV) and Au foils (Au 4f7/2 = 83.96 eV).[58] Peaks were charge referenced to CHx band in the carbon 1s spectra at 284.8 eV. Measurements were made at a takeoff angle of 45° with respect to the sample surface plane. This resulted in a typical sampling depth of 3−6 nm (95% of the signal originated from this depth or shallower). Quantification was done using instrumental relative sensitivity factors (RSFs) that account for the X-ray cross section and inelastic mean free path of the electrons.

Computational Methods. Geometry relaxations of the candidate crystal structures were performed by density functional theory implemented in the VASP package.[59] The calculations were done using the PBE exchange-correlation functional.[60,61] Dispersion correction was included by the Becke-Johnson damping DFT-D3(BJ) method of Grimme.[62,63] The energy cutoff for the plane-wave basis was 600 eV. A 0.2 eV Gaussian smearing and a k point mesh of 0.5 $Å^{-1}$ were used. Simulated X-ray diffraction patterns were calculated using the SingleCrystal software. [4 + 2] Cycloaddition barriers and reaction energies are computed at the B3LYP[64,65]/6-31G(d)[66] level of theory using Gaussian 09.[67]

Three types of enumerated furan nanothreads, *syn*, *anti*, and *syn/anti*, were optimized in a $20 \times 20 \times c$ Å (c is the periodicity along the thread axis) tetragonal unit cell with a convergence force threshold for ionic minimization 10−5 Ry/au. The IR absorption spectra for those optimized structures were then calculated within density functional theory using the PBE exchange-correlation functional implemented in Quantum Espresso packages.[68,69] The self-consistency threshold for the vibrational frequencies calculation was 10−16 Ry. The acoustic sum rules were imposed in order to correct the negative acoustic modes owing to finite plane-wave cutoff. The calculated frequencies were scaled by a factor of 0.98.

Optical Microscopy. Optical microscopy images were collected using an Olympus BX61 optical microscope with crossed polarizers with a 530 nm full waveplate.

ASSOCIATED CONTENT

Supporting Information

The Supporting Information is available free of charge at https://pubs.acs.org/doi/10.1021/acsnano.0c10400.

X-ray data for B-1-a (CIF)
X-ray data for B-2-a (CIF)
X-ray data for B-1-b (CIF)
X-ray data for C-1-a (CIF)
X-ray data for C-2-a (CIF)
Calculated [4 + 2] cycloaddition barriers and reaction energies, *in situ* X-ray diffraction of single-crystal furan, packing arrangements of ellipses and axial shift of nanothreads considered, simulated packings of furan-derived nanothreads, comparison of experimental and simulated 6-fold diffraction pattern of the C-2-a *anti*-furan nanothread packing; XPS, Raman, reflectance infrared spectra, and mass spectra of PE press solid; WAXS and in-house X-ray diffraction patterns of PE press solid; calculated relative enthalpies/volume/*d*-spacings of the packed furan nanothreads, comparison of experimental and simulated infrared spectra (PDF)

AUTHOR INFORMATION

Corresponding Author

Elizabeth Elacqua − *Department of Chemistry and Materials Research Institute, The Pennsylvania State University, University Park, Pennsylvania 16802, United States;* orcid.org/0000-0002-1239-9560; Email: elizabeth.elacqua@psu.edu

Authors

Steven Huss − *Department of Chemistry, The Pennsylvania State University, University Park, Pennsylvania 16802, United States;* orcid.org/0000-0001-6244-4406

Sikai Wu − *Department of Chemistry, The Pennsylvania State University, University Park, Pennsylvania 16802, United States;* orcid.org/0000-0001-6041-6436

Bo Chen − *Department of Chemistry, The Pennsylvania State University, University Park, Pennsylvania 16802, United States; Department of Chemistry and Chemical Biology, Cornell University, Ithaca, New York 14853, United States; Donostia International Physics Center, Paseo Manuel de Lardizabal, 4, 20018 Donostia, San Sebastian, Spain; Basque Foundation for Science, 48013 Bilbao, Spain*

Tao Wang − *Department of Physics and Department of Mechanical Engineering, The Pennsylvania State University, University Park, Pennsylvania 16802, United States;* orcid.org/0000-0003-2833-1592

Margaret C. Gerthoffer − *Department of Chemistry, The Pennsylvania State University, University Park, Pennsylvania 16802, United States;* orcid.org/0000-0001-5015-0128

Daniel J. Ryan − *ExxonMobil Research and Engineering Company, Annandale, New Jersey 08801, United States;* orcid.org/0000-0001-8201-1472

Stuart E. Smith − *ExxonMobil Research and Engineering Company, Annandale, New Jersey 08801, United States;* orcid.org/0000-0003-2785-1393

Vincent H. Crespi − *Department of Chemistry, Materials Research Institute, Department of Physics, and Department of Materials Science and Engineering, The Pennsylvania State University, University Park, Pennsylvania 16802, United States*

[Δ]**John V. Badding** − *Department of Chemistry, Materials Research Institute, Department of Physics, and Department of Materials Science and Engineering, The Pennsylvania State University, University Park, Pennsylvania 16802, United States;* orcid.org/0000-0002-4517-830X

Complete contact information is available at: https://pubs.acs.org/10.1021/acsnano.0c10400

Notes

The authors declare no competing financial interest.
[Δ](J.V.B.) Deceased October 26, 2019.
This article was previously submitted to ChemRxiv.[70] Since then, wide-angle X-ray scattering (WAXS), high-resolution matrix-assisted laser desorption/ionization (MALDI) mass spectrometry, and infrared spectra of the recovered solid before and after air exposure have been added.

ACKNOWLEDGMENTS

This work was funded by the Center for Nanothread Chemistry, a National Science Foundation (NSF) Center for Chemical Innovation (CHE-1832471). The authors thank ExxonMobil Research and Engineering Co. for financial support. We acknowledge R. Hoffmann and R. Schaak for insights and helpful discussions throughout the preparation of this manuscript. We thank M. Gopinadhan at ExxonMobil Research and Engineering Co. for many helpful discussions. We thank C. Park, D. Popov, and J. Smith of the Advanced

Photon Source, Argonne National Laboratory for assistance with X-ray diffraction measurements. Infrared Spectroscopy was performed at the Materials Characterization Lab in the Materials Research Institute at the Pennsylvania State University. We thank J. Shallenberger of the Materials Characterization Lab in the Materials Research Institute at the Pennsylvania State University for assistance with XPS measurements. We acknowledge the computing resource provided by the Extreme Science and Engineering Discovery Environment (XSEDE) Comet cluster at the San Diego Supercomputer Center through allocation CHE180059.

REFERENCES

(1) Dresselhaus, M. S.; Dresselhaus, G.; Eklund, P. C. Structure of Fullerenes. *Science of Fullerenes and Carbon Nanotubes*, 1st ed.; Academic Press: San Diego, 1996; p 60.

(2) Kroto, H. W.; Heath, J. R.; O'Brien, S. C.; Curl, R. F.; Smalley, R. E. C60: Buckminsterfullerene. *Nature* **1985**, *318*, 162−163.

(3) Iijima, S. Helical Microtubules of Graphitic Carbon. *Nature* **1991**, *354*, 56−58.

(4) Charlier, J.-C.; Blase, X.; Roche, S. Electronic and Transport Properties of Nanotubes. *Rev. Mod. Phys.* **2007**, *79*, 677−732.

(5) Golder, M. R.; Jasti, R. Syntheses of the Smallest Carbon Nanohoops and the Emergence of Unique Physical Phenomena. *Acc. Chem. Res.* **2015**, *48*, 557−566.

(6) Leonhardt, E. J.; Jasti, R. Emerging Applications of Carbon Nanohoops. *Nat. Rev. Chem.* **2019**, *3*, 672−686.

(7) Van Raden, J. M.; Leonhardt, E. J.; Zakharov, L. N.; Pérez-Guardiola, A.; Pérez-Jiménez, A. J.; Marshall, C. R.; Brozek, C. K.; Sancho-García, J. C.; Jasti, R. Precision Nanotube Mimics *via* Self-Assembly of Programmed Carbon Nanohoops. *J. Org. Chem.* **2020**, *85*, 129−141.

(8) Sofo, J. O.; Chaudhari, A. S.; Barber, G. D. Graphane: A Two-Dimensional Hydrocarbon. *Phys. Rev. B: Condens. Matter Mater. Phys.* **2007**, *75*, 153401.

(9) Wen, X.-D.; Hand, L.; Labet, V.; Yang, T.; Hoffmann, R.; Ashcroft, N. W.; Oganov, A. R.; Lyakhov, A. O. Graphane Sheets and Crystals Under Pressure. *Proc. Natl. Acad. Sci. U. S. A.* **2011**, *108*, 6833−6837.

(10) Strauss, M. J.; Asheghali, D.; Evans, A. M.; Li, R. L.; Chavez, A. D.; Sun, C.; Becker, M. L.; Dichtel, W. R. Cooperative Self-Assembly of Pyridine-2,6-Diimine-Linked Macrocycles into Mechanically Robust Nanotubes. *Angew. Chem., Int. Ed.* **2019**, *58*, 14708−14714.

(11) Vitaku, E.; Gannett, C. N.; Carpenter, K. L.; Shen, L.; Abruña, H. D.; Dichtel, W. R. Phenazine-Based Covalent Organic Framework Cathode Materials with High Energy and Power Densities. *J. Am. Chem. Soc.* **2020**, *142*, 16−20.

(12) Meng, Z.; Stolz, R. M.; Mirica, K. A. Two-Dimensional Chemiresistive Covalent Organic Framework with High Intrinsic Conductivity. *J. Am. Chem. Soc.* **2019**, *141*, 11929−11937.

(13) Zhu, T.; Ertekin, E. Phonons, Localization, and Thermal Conductivity of Diamond Nanothreads and Amorphous Graphene. *Nano Lett.* **2016**, *16*, 4763−4772.

(14) Zhan, H.; Zhang, G.; Zhang, Y.; Tan, V. B. C.; Bell, J. M.; Gu, Y. Thermal Conductivity of a New Carbon Nanotube Analog: The Diamond Nanothread. *Carbon* **2016**, *98*, 232−237.

(15) Zhan, H.; Gu, Y. Thermal Conductivity of Diamond Nanothread. *Thermal Transport in Carbon-Based Nanomaterials*, 1st ed.; Elsevier: New York, 2017; pp 185−204.

(16) Fitzgibbons, T. C.; Guthrie, M.; Xu, E. S.; Crespi, V. H.; Davidowski, S. K.; Cody, G. D.; Alem, N.; Badding, J. V. Benzene-Derived Carbon Nanothreads. *Nat. Mater.* **2015**, *14*, 43−47.

(17) Li, X.; Baldini, M.; Wang, T.; Chen, B.; Xu, E.; Vermilyea, B.; Crespi, V. H.; Hoffmann, R.; Molaison, J. J.; Tulk, C. A.; Guthrie, M.; Sinogeikin, S.; Badding, J. V. Mechanochemical Synthesis of Carbon Nanothread Single Crystals. *J. Am. Chem. Soc.* **2017**, *139*, 16343−16349.

(18) Li, X.; Wang, T.; Duan, P.; Baldini, M.; Huang, H.-T.; Chen, B.; Juhl, S. J.; Koeplinger, D.; Crespi, V. H.; Schmidt-Rohr, K.; Hoffmann, R.; Alem, N.; Guthrie, M.; Zhang, X.; Badding, J. V. Carbon Nitride Nanothread Crystals Derived from Pyridine. *J. Am. Chem. Soc.* **2018**, *140*, 4969−4972.

(19) Biswas, A.; Ward, M. D.; Wang, T.; Zhu, L.; Huang, H.-T.; Badding, J. V.; Crespi, V. H.; Strobel, T. A. Evidence for Orientational Order in Nanothreads Derived from Thiophene. *J. Phys. Chem. Lett.* **2019**, *10*, 7164−7171.

(20) Tang, W. S.; Strobel, T. A. Evidence for Functionalized Carbon Nanothreads from π-Stacked, Para-Disubstituted Benzenes. *J. Phys. Chem. C* **2020**, *124*, 25062−25070.

(21) Friedrich, A.; Collings, I. E.; Dziubek, K. F.; Fanetti, S.; Radacki, K.; Ruiz-Fuertes, J.; Pellicer-Porres, J.; Hanfland, M.; Sieh, D.; Bini, R.; Clark, S. J.; Marder, T. B. Pressure-Induced Polymerization of Polycyclic Arene-Perfluoroarene Cocrystals: Single Crystal X-Ray Diffraction Studies, Reaction Kinetics, and Design of Columnar Hydrofluorocarbons. *J. Am. Chem. Soc.* **2020**, *142*, 18907−18923.

(22) Roman, R. E.; Kwan, K.; Cranford, S. W. Mechanical Properties and Defect Sensitivity of Diamond Nanothreads. *Nano Lett.* **2015**, *15*, 1585−1590.

(23) Silveira, J. F. R. V.; Muniz, A. R. First-Principles Calculation of the Mechanical Properties of Diamond Nanothreads. *Carbon* **2017**, *113*, 260−265.

(24) Zhan, H.; Zhang, G.; Tan, V. B. C.; Cheng, Y.; Bell, J. M.; Zhang, Y.-W.; Gu, Y. From Brittle to Ductile: A Structure Dependent Ductility of Diamond Nanothread. *Nanoscale* **2016**, *8*, 11177−11184.

(25) Chen, M.-M.; Xiao, J.; Cao, C.; Zhang, D.; Cui, L.-L.; Xu, X.-M.; Long, M.-Q. Theoretical Prediction Electronic Properties of Group-IV Diamond Nanothreads. *AIP Adv.* **2018**, *8*, 075107.

(26) Zhan, H.; Zhang, G.; Tan, V. B. C.; Gu, Y. The Best Features of Diamond Nanothread for Nanofibre Applications. *Nat. Commun.* **2017**, *8*, 14863.

(27) Elacqua, E.; Kaushik, P.; Groeneman, R. H.; Sumrak, J. C.; Bučar, D.-K.; MacGillivray, L. R. A Supramolecular Protecting Group Strategy Introduced to the Organic Solid State: Enhanced Reactivity through Molecular Pedal Motion. *Angew. Chem., Int. Ed.* **2012**, *51*, 1037−1041.

(28) Maryasin, B.; Olbrich, M.; Trauner, D.; Ochsenfeld, C. Calculated Nuclear Magnetic Resonance Spectra of Polytwistane and Related Hydrocarbon Nanorods. *J. Chem. Theory Comput.* **2015**, *11*, 1020−1026.

(29) Duan, P.; Li, X.; Wang, T.; Chen, B.; Juhl, S. J.; Koeplinger, D.; Crespi, V. H.; Badding, J. V.; Schmidt-Rohr, K. The Chemical Structure of Carbon Nanothreads Analyzed by Advanced Solid-State NMR. *J. Am. Chem. Soc.* **2018**, *140*, 7658−7666.

(30) Hess, B. A.; Schaad, L. J. Hückel Molecular Orbital Π Resonance Energies. The Benzenoid Hydrocarbons. *J. Am. Chem. Soc.* **1971**, *93*, 2413−2416.

(31) Hess, B. A. A.; Schaad, L. J. J.; Holyoke, C. W. W. The Aromaticity of Heterocycles Containing the Imine Nitrogen. *Tetrahedron* **1975**, *31*, 295−298.

(32) Guo, L.; Wang, G.; Yan, Z.; Zhang, X. Mechanism for Covalent Dimerization of Pyridine: [4 + 2] Dimerization, an MP2 Investigation. *Chem. Phys. Lett.* **2016**, *644*, 132−137.

(33) Gerthoffer, M. C.; Wu, S.; Chen, B.; Wang, T.; Huss, S.; Oburn, S. M.; Crespi, V. H.; Badding, J. V.; Elacqua, E. 'Sacrificial' Supramolecular Assembly and Pressure-Induced Polymerization: Toward Sequence-Defined Functionalized Nanothreads. *Chem. Sci.* **2020**, *11*, 11419−11424.

(34) Hess, B. A.; Schaad, L. J.; Holyoke, C. W. On the Aromaticity of Heterocycles Containing the Amine Nitrogen or the Ether Oxygen. *Tetrahedron* **1972**, *28*, 3657−3667.

(35) Chen, B.; Hoffmann, R.; Ashcroft, N. W.; Badding, J.; Xu, E.; Crespi, V. Linearly Polymerized Benzene Arrays as Intermediates, Tracing Pathways to Carbon Nanothreads. *J. Am. Chem. Soc.* **2015**, *137*, 14373−14386.

https://dx.doi.org/10.1021/acsnano.0c10400

(36) Ceppatelli, M.; Santoro, M.; Bini, R.; Schettino, V. High Pressure Reactivity of Solid Furan Probed by Infrared and Raman Spectroscopy. *J. Chem. Phys.* **2003**, *118*, 1499−1506.

(37) Chen, B.; Hoffmann, R.; Cammi, R. The Effect of Pressure on Organic Reactions in Fluids—A New Theoretical Perspective. *Angew. Chem., Int. Ed.* **2017**, *56*, 11126−11142.

(38) Sinogeikin, S. V.; Smith, J. S.; Rod, E.; Lin, C.; Kenney-Benson, C.; Shen, G. Online Remote Control Systems for Static and Dynamic Compression and Decompression Using Diamond Anvil Cells. *Rev. Sci. Instrum.* **2015**, *86*, 072209.

(39) Nobrega, M. M.; Teixeira-Neto, E.; Cairns, A. B.; Temperini, M. L. A.; Bini, R. One-Dimensional Diamondoid Polyaniline-Like Nanothreads from Compressed Crystal Aniline. *Chem. Sci.* **2018**, *9*, 254−260.

(40) Ward, M. D.; Tang, W. S.; Zhu, L.; Popov, D.; Cody, G. D.; Strobel, T. A. Controlled Single-Crystalline Polymerization of $C_{10}H_8\eta C_{10}F_8$ under Pressure. *Macromolecules* **2019**, *52*, 7557−7563.

(41) Grunbaum, B.; Shephard, G. C. Ellipse Patterns. *Tilings and Patterns*, 1st ed.; W. H. Freeman and Company: New York, 1987; pp 375−389.

(42) Klots, T. D.; Chirico, R. D.; Steele, W. V. Complete Vapor Phase Assignment for the Fundamental Vibrations of Furan, Pyrrole and Thiophene. *Spectrochim. Acta, Part A* **1994**, *50*, 765−795.

(43) Rico, M.; Barrachina, M.; Orza, J. M. Fundamental Vibrations of Furan and Deuterated Derivatives. *J. Mol. Spectrosc.* **1967**, *24*, 133−148.

(44) Pruzan, P.; Chervin, J. C.; Thiéry, M. M.; Itié, J. P.; Besson, J. M.; Forgerit, J. P.; Revault, M. Transformation of Benzene to a Polymer after Static Pressurization to 30 GPa. *J. Chem. Phys.* **1990**, *92*, 6910−6915.

(45) Ciabini, L.; Santoro, M.; Bini, R.; Schettino, V. High Pressure Reactivity of Solid Benzene Probed by Infrared Spectroscopy. *J. Chem. Phys.* **2002**, *116*, 2928−2935.

(46) Juhl, S. J.; Wang, T.; Vermilyea, B.; Li, X.; Crespi, V. H.; Badding, J. V.; Alem, N. Local Structure and Bonding of Carbon Nanothreads Probed by High-Resolution Transmission Electron Microscopy. *J. Am. Chem. Soc.* **2019**, *141*, 6937−6945.

(47) Fang, J.; Bull, C. L.; Loveday, J. S.; Nelmes, R. J.; Kamenev, K. V. Strength Analysis and Optimisation of Double-Toroidal Anvils for High-Pressure Research. *Rev. Sci. Instrum.* **2012**, *83*, 093902.

(48) Loveday, J. S.; Nelmes, R. J. High-Pressure Gas Hydrates. *Phys. Chem. Chem. Phys.* **2008**, *10*, 937−950.

(49) Molin, L.; Seraglia, R.; Czarnocki, Z.; Maurin, J. K.; Pluciński, F. A.; Traldi, P. On the Primary Ionization Mechanism(s) in Matrix-Assisted Laser Desorption Ionization. *J. Anal. Methods Chem.* **2012**, *2012*, 1−8.

(50) Ryan, D. J.; Qian, K. Laser-Based Ionization: A Review on the Use of Matrix-Assisted Laser Desorption/Ionization and Laser Desorption/Ionization Mass Spectrometry in Petroleum Research. *Energy Fuels* **2020**, *34*, 11887−11896.

(51) Prentice, B. M.; Ryan, D. J.; Van de Plas, R.; Caprioli, R. M.; Spraggins, J. M. Enhanced Ion Transmission Efficiency up to m/z 24 000 for MALDI Protein Imaging Mass Spectrometry. *Anal. Chem.* **2018**, *90*, 5090−5099.

(52) Ryan, D. J.; Nei, D.; Prentice, B. M.; Rose, K. L.; Caprioli, R. M.; Spraggins, J. M. Protein Identification in Imaging Mass Spectrometry through Spatially Targeted Liquid Micro-Extractions. *Rapid Commun. Mass Spectrom.* **2018**, *32*, 442−450.

(53) Hrubiak, R.; Sinogeikin, S.; Rod, E.; Shen, G. The Laser Micro-Machining System for Diamond Anvil Cell Experiments and General Precision Machining Applications at the High Pressure Collaborative Access Team. *Rev. Sci. Instrum.* **2015**, *86*, 072202.

(54) Dewaele, A.; Torrent, M.; Loubeyre, P.; Mezouar, M. Compression Curves of Transition Metals in the Mbar Range: Experiments and Projector Augmented-Wave Calculations. *Phys. Rev. B: Condens. Matter Mater. Phys.* **2008**, *78*, 104102.

(55) Besson, J. M.; Nelmes, R. J.; Hamel, G.; Loveday, J. S.; Weill, G.; Hull, S. Neutron Powder Diffraction above 10 GPa. *Phys. B* **1992**, *180−181*, 907−910.

(56) Klotz, S. *Techniques in High Pressure Neutron Scattering*; CRC Press: Boca Raton, 2012.

(57) Prescher, C.; Prakapenka, V. B. DIOPTAS: A Program for Reduction of Two-Dimensional X-Ray Diffraction Data and Data Exploration. *High Pressure Res.* **2015**, *35*, 223−230.

(58) Seah, M. P. Summary of ISO/TC 201 Standard: VII ISO 15472:2001 - Surface Chemical Analysis - X-Ray Photoelectron Spectrometers - Calibration of Energy Scales. *Surf. Interface Anal.* **2001**, *31*, 721−723.

(59) Kresse, G.; Furthmüller, J. Efficient Iterative Schemes for *ab Initio* Total-Energy Calculations Using a Plane-Wave Basis Set. *Phys. Rev. B: Condens. Matter Mater. Phys.* **1996**, *54*, 11169−11186.

(60) Perdew, J. P.; Burke, K.; Ernzerhof, M. Generalized Gradient Approximation Made Simple. *Phys. Rev. Lett.* **1996**, *77*, 3865−3868.

(61) Perdew, J. P.; Burke, K.; Ernzerhof, M. Generalized Gradient Approximation Made Simple. *Phys. Rev. Lett.* **1996**, *77*, 3865; *Phys. Rev. Lett.* **1997**, *78*, 1396−1396.

(62) Grimme, S.; Antony, J.; Ehrlich, S.; Krieg, H. A Consistent and Accurate *ab Initio* Parametrization of Density Functional Dispersion Correction (DFT-D) for the 94 Elements H-Pu. *J. Chem. Phys.* **2010**, *132*, 154104.

(63) Grimme, S.; Ehrlich, S.; Goerigk, L. Effect of the Damping Function in Dispersion Corrected Density Functional Theory. *J. Comput. Chem.* **2011**, *32*, 1456−1465.

(64) Becke, A. D. Density-Functional Thermochemistry. III. The Role of Exact Exchange. *J. Chem. Phys.* **1993**, *98*, 5648−5652.

(65) Lee, C.; Yang, W.; Parr, R. G. Development of the Colle-Salvetti Correlation-Energy Formula into a Functional of the Electron Density. *Phys. Rev. B: Condens. Matter Mater. Phys.* **1988**, *37*, 785−789.

(66) Hariharan, P. C.; Pople, J. A. The Influence of Polarization Functions on Molecular Orbital Hydrogenation Energies. *Theor. Chim. Acta* **1973**, *28*, 213−222.

(67) Frisch, M. J.; Trucks, G. W.; Schlegel, H. B.; Scuseria, G. E.; Robb, M. A.; Cheeseman, J. R.; Scalmani, G.; Barone, V.; Mennucci, B.; Petersson, G. A.; Nakatsuji, H.; Caricato, M.; Li, X.; Hratchian, H. P.; Izmaylov, A. F.; Bloino, J.; Zheng, G.; Sonnenberg, J. L.; Hada, M.; Ehara, M.; et al. *Gaussian 09*, Revision D.01; Gaussian, Inc.: Wallingford, CT, 2009.

(68) Giannozzi, P.; Andreussi, O.; Brumme, T.; Bunau, O.; Buongiorno Nardelli, M.; Calandra, M.; Car, R.; Cavazzoni, C.; Ceresoli, D.; Cococcioni, M.; Colonna, N.; Carnimeo, I.; Dal Corso, A.; De Gironcoli, S.; Delugas, P.; Distasio, R. A.; Ferretti, A.; Floris, A.; Fratesi, G.; Fugallo, G.; et al. Advanced Capabilities for Materials Modelling with Quantum ESPRESSO. *J. Phys.: Condens. Matter* **2017**, *29*, 465901.

(69) Giannozzi, P.; Baroni, S.; Bonini, N.; Calandra, M.; Car, R.; Cavazzoni, C.; Ceresoli, D.; Chiarotti, G. L.; Cococcioni, M.; Dabo, I.; Dal Corso, A.; De Gironcoli, S.; Fabris, S.; Fratesi, G.; Gebauer, R.; Gerstmann, U.; Gougoussis, C.; Kokalj, A.; Lazzeri, M.; Martin-Samos, L.; et al. QUANTUM ESPRESSO: A Modular and Open-Source Software Project for Quantum Simulations of Materials. *J. Phys.: Condens. Matter* **2009**, *21*, 395502.

(70) Huss, S.; Wu, S.; Chen, B.; Wang, T.; Gerthoffer, M. C.; Hoffmann, R.; Crespi, V. H.; Badding, J. V.; Elacqua, E. Scalable Synthesis of Crystalline One-Dimensional Carbon Nanothreads through Modest-Pressure Polymerization of Furan. *ChemRxiv* 2020, https://chemrxiv.org/articles/preprint/Scalable_Synthesis_of_Crystalline_One-Dimensional_Carbon_Nanothreads_Through_Modest-Pressure_Polymerization_of_Furan/12341057/1 (accessed 2021-01-07).